Computer Modeling in Engineering & Sciences

Tech Science Press

DOI: 10.32604/cmes.2021.014284

ARTICLE

Impacts of Disk Rock Sample Geometric Dimensions on Shear Fracture Behavior in a Punch Shear Test

Tantan Zhu* **and Yao Li**

School of Highway, Chang'an University, Xi'an, 710064, China

*Corresponding Author: Tantan Zhu. Email: tantan.zhu@chd.edu.cn

Received: 15 September 2020 Accepted: 03 December 2020

ABSTRACT

Punch shear tests have been widely used to determine rock shear mechanical properties but without a standard sample geometric dimension suggestion. To investigate the impacts of sample geometric dimensions on shear behaviors in a punch shear test, simulations using Particle Flow Code were carried out. The effects of three geometric dimensions (i.e., disk diameter, ratio of shear surface diameter to disk diameter, and ratio of disk height to shear surface diameter) were discussed. Variations of shear strength, shear stiffness, and shear dilatancy angles were studied, and the fracture processes and patterns of samples were investigated. Then, normal stress on the shear surface during test was analyzed and a suggested disk geometric dimension was given. Simulation results show that when the ratio of the shear surface diameter to the disk diameter and the ratio of disk height to the shear surface diameter is small enough, the shear strength, shear stiffness, and shear dilatancy angles are extremely sensitive to the three geometric parameters. If the ratio of surface diameter to disk diameter is too large or the ratio of disk height to surface diameter is too small, a part of the sample within the shear surface will fail due to macro tensile cracks, which is characterized by break off. Samples with a greater ratio of disk height to shear surface diameter, namely when the sample is relatively thick, crack from one end to the other while others crack from both ends towards the middle. During test, the actual normal stress on the shear surface is greater than the target value because of the extra compressive stress from the part of sample outside shear surface.

KEYWORDS

Punch shear test; shear behavior; suggested geometric dimensions; particle flow code simulation; fracture process

1 Introduction

Shear fracture is one of the fundamental failure patterns of rocks. At present, Mohr–Coulomb criterion is widely used for the determination of shear strength and the envelope, which intercepts the τ-axis at cohesion with a slope equal to internal friction angle, is assumed to be a straight line in the $\tau - \sigma_n$ plane [1–3]. The internal friction angle and cohesion, which are based on Mohr–Coulomb theory, are important shear mechanical parameters used for rock engineering design [4,5]. These shear mechanical parameters are mainly determined by triaxial compression tests [6–8] or direct shear tests (DST) [9–12].

This work is licensed under a Creative Commons Attribution 4.0 International License, which permits unrestricted use, distribution, and reproduction in any medium, provided the original work is properly cited.

In a triaxial compression test, the sample fails under axial and confining stresses. The strength envelope can be obtained by the tangent line of the Mohr's stress circles based on minimum and maximum principal stresses [13,14]. However, the normal and shear stresses on the shear plane cannot be directly obtained from triaxial compression test results. Unlike the triaxial compression test, the DST can directly measure the normal and shear stresses on the shear plane [15,16]. There are two commonly used methods in this category: Direct shear-box test and punch shear test (PST). For the direct shear-box test, upper and lower shear boxes are the main component of the shear device. Samples in the shear-box test are subjected to normal and shears stresses and fails along an approximate plane. However, when the sample is subjected to the PST, it fails along a cylindrical surface rather than a plane (as shown in Fig. 1). Originally, the PST was proposed for conveniently determining the direct shear strength [17]. Shear stress is applied by a compressive force within and parallel to the shear surface during the PST. The PST is applicable for high strength solids, minimizes the bending stress on the samples, and facilitates sample preparation [17,18]. Thus, other testing methods, such as the punch through shear test which uses a rock disk sample with two circular notches, was proposed based on the PST to determine shear mechanical parameters [19–21].

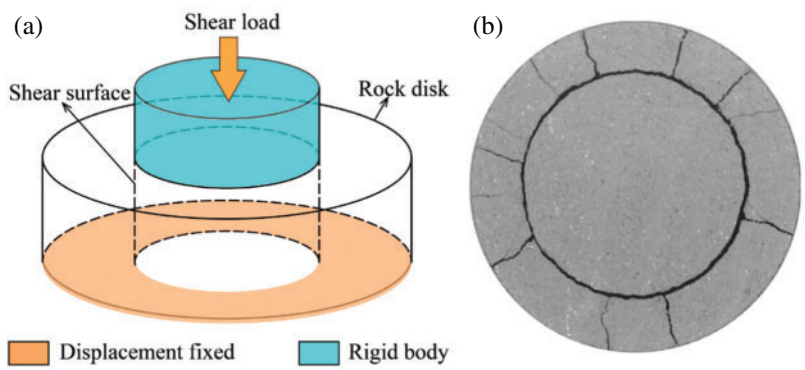

Figure 1: Punch shear test: (a) Schematic diagram; (b) Fracture pattern [22]

Rock sample dimensions in laboratory tests significantly impact the test result. As shown in Fig. 2, the tested sample in the PST has three important geometric dimensions, disk diameter (D), shear surface diameter (D_i), and disk height (H), all of which influence the test result. However, unlike the uniaxial and triaxial compression test, which use a cylindrical sample with a height-diameter ratio of two, no standard sample size is specified for the PST. For example, Xu et al. [22] used disk samples with the $D = 38$ mm, $D_i = 25.4$ mm, and $H = 15$ mm to carry out a PST for the investigation of dynamic shear response of rocks. Huang et al. [23] also carried out a PST under a dynamic load, but the dimensions of their samples were $D = 57$ mm, $D_i = 25$ mm, and $H = 14$ mm. Backers et al. [24] conducted a punch through shear test using disks with the $D = 50$ mm and $D_i = 25$ mm. As the geometric dimensions of the samples used in these studies are different, the results are not directly comparable. Therefore, the influence of the sample dimensions on shear behavior should be analyzed further and a standard sample dimension should be created for PST.

To investigate the influence of the geometric dimensions of the sample disk on the shear behavior of rocks in the PST, punch shear simulations were carried out under zero normal stress by using Particle Flow Code (PFC). Variations in shear mechanical parameters under various

geometries were studied. Then, the failure process and fracture pattern of disks with different disk dimensions were investigated. Finally, the normal stress on the shear surface during the test was analyzed and a suggested disk size was given.

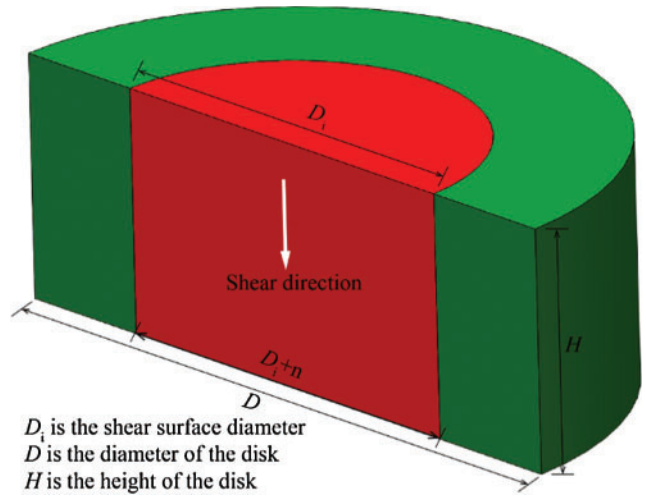

Figure 2: Geometrical dimensions of the disk used for PST (half of the disk)

2 Particle Flow Code and Simulation Methodology

2.1 Particle Flow Code

PFC^{3D}, a three-dimensional discrete element modeling framework, has been widely used in rock mechanical simulations. The model framework simplifies rock material into balls and bonds. A ball in the PFC^{3D} is a rigid and the surface of the ball is defined by radius. A ball has a single set of surface properties. Balls can translate and rotate. As linear parallel-bond can transmit both force and moment while contact-bond only transmits force [25–27], it was selected to conduct the PST simulations. For the parallel-bond, the contact force and moment are updated as follows:

$$F_c = F^l + F^d + \overline{F} \tag{1}$$

$$M_c = \overline{M} \tag{2}$$

where F_c is contact force; F^l and F^d is linear force and dashpot force, respectively; $\overline{F}$ is parallel-bond force; M_c is contact moment; $\overline{M}$ is parallel-bond moment. The parallel-bond contact force consists of a normal force $\overline{F}_n$ and a shear force $\overline{F}_s$, and the parallel-bond moment consists of a twisting moment $\overline{M}_t$ and a bending moment $\overline{M}_b$:

$$\overline{F} = -\overline{F}_n \vec{n}_c + \overline{F}_s \tag{3}$$

$$\overline{M} = \overline{M}_t \vec{n}_c + \overline{M}_b \tag{4}$$

where n_c is the direction of the contact plane. The parallel-bond shear force and bending moment line on the contact and are expressed as:

$$\overline{F}_{\mathrm{s}} = -\overline{F}_{\mathrm{ss}}\vec{\overline{s}}_{\mathrm{c}} + \overline{F}_{\mathrm{st}}\overline{t}_{\mathrm{c}} \tag{5}$$

$$\overline{M}_{\mathrm{b}} = \overline{M}_{\mathrm{bs}}\overline{s}_{\mathrm{c}} + \overline{M}_{\mathrm{bt}}\overline{t}_{\mathrm{c}} \tag{6}$$

The force–displacement law for the parallel-bond force and moment consists of the following seven steps.

(1) Update the bond cross-sectional properties. In this step, the radius R, cross-sectional area A, moment of inertia I, the polar moment of inertia J of parallel-bond will be calculated:

$$A = \pi R^2 \tag{7}$$

$$I = \frac{1}{4}\pi R^4 \tag{8}$$

$$J = \frac{1}{2}\pi R^4 \tag{9}$$

(2) Update normal force. The normal force will be recalculated according to the relative normal-displacement increment $\Delta\delta_{\mathrm{n}}$, normal stiffness of the parallel-bond k_{n}, and the area of the parallel A:

$$\overline{F}_{\mathrm{n}} = \overline{F}_{\mathrm{n}} + k_{\mathrm{n}} A \Delta\delta_{\mathrm{n}} \tag{10}$$

(3) Update shear force. Shear force of the parallel-bond will be recalculated in this step:

$$\overline{F}_{\mathrm{s}} = \overline{F}_{\mathrm{s}} + k_{\mathrm{s}} A \Delta\delta_{\mathrm{s}} \tag{11}$$

where k_s is shear stiffness of the parallel-bond and $\Delta\delta_{\mathrm{s}}$ is the relative shear–displacement increment.

(4) Update twisting moment:

$$\overline{M}_{\mathrm{t}} = \overline{M}_{\mathrm{t}} - k_{\mathrm{s}} J \Delta\theta_{\mathrm{t}} \tag{12}$$

where $\Delta\theta_{\mathrm{t}}$ is a relative twist-rotation increment.

(5) Update bending moment:

$$\overline{M}_{\mathrm{b}} = \overline{M}_{\mathrm{b}} - k_{\mathrm{n}} I \Delta\theta_{\mathrm{b}} \tag{13}$$

where $\Delta\theta_{\mathrm{b}}$ is relative bend-rotation increment.

(6) Update the maximum normal and shear stresses at the parallel-bond periphery:

$$\sigma_{\mathrm{n}} = \frac{\overline{F}_{\mathrm{n}}}{A} + \beta\frac{\|\|R}{I}, \quad \tau = \frac{\|\overline{F}_{\mathrm{s}}\|}{A} + \beta\frac{|M_{\mathrm{t}}|R}{J} \tag{14}$$

where β is moment-contribution factor.

(7) Enforce strength limits. If the tensile strength limit of the parallel-bond is exceeded, then break the bond in tension. If the shear strength limit of the parallel-bond is exceeded, then break the bond in shear.

2.2 Simulation Methodology

In PFC^{3D}, stress is applied within the model by moving walls or balls. If the tensile or shear strength of a bond is exceeded, a tensile or shear micro-crack will be formed. The numerical model in this study is composed of five walls (Fig. 3a). The diameter of the first wall (Wall #1), a circular wall, is equal to the D_i. The second wall (Wall #2) is in the shape of a ring and has an outer diameter larger than the D and an inner diameter smaller than the D_i. The diameter of the third wall (Wall #3) is larger than D_i+n. The inner diameter of the fourth wall (Wall #4) is equal to the D_i of the sample plus an additional four millimeters, and with an outer diameter larger than the D The fifth wall (Wall #5) is a cylindrical wall with a diameter equal to the D. These five walls ensure that the simulated rock material does not leave the domain (Fig. 3b). Once the simulated rock material was bonded by contacts (Fig. 3c), Wall #2 and #3 were removed from the model domain before finalizing the numerical model and applying displacement and stress. According to Xu et al. [22] and Huang et al. [23], the shear surface is not a standard cylinder, with the bottom diameter of the shear cylinder slightly larger than the top diameter. Shear stress on the shear surface can be calculated by dividing the shear force by the area of the shear surface. In the PST, the average diameter of the shear surface is $(2D_i+n)/2$. Thus, the shear stress on the shear surface can be calculated as:

$$\tau = \frac{2P}{\pi H\,(2D_{\mathrm{i}}+n)} \tag{15}$$

where P is the shear load and n are the difference between the top diameter and bottom diameter of the shear surface.

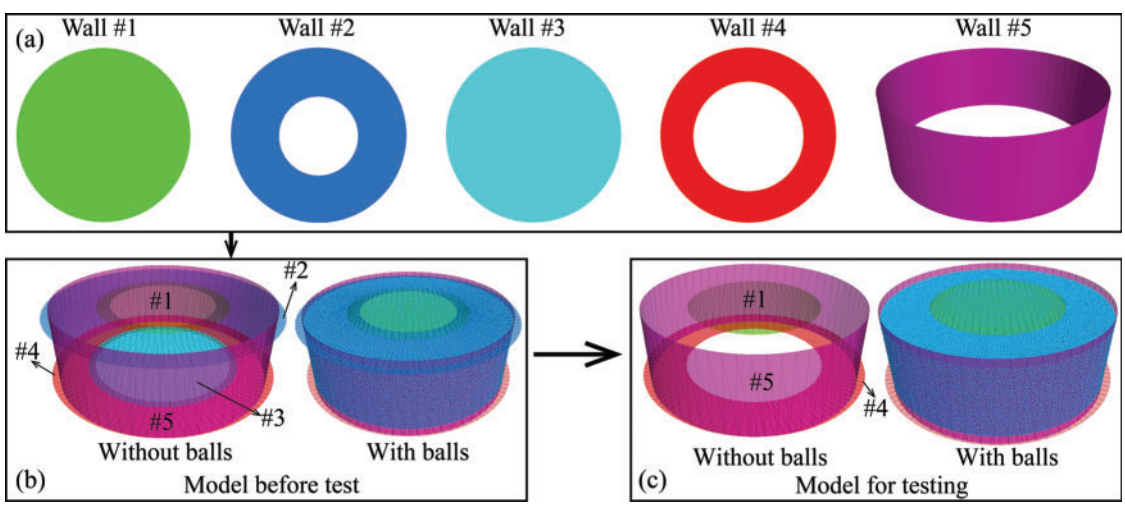

Figure 3: Numerical model of the disk used for simulation (a) shows the shapes of the walls; (b) is the numerical sample with all the walls; (c) is the numerical sample with the walls #2 and #3 deleted

As the strength of a parallel-bond conforms to the Mohr–Coulomb criterion. Therefore, the strength of a parallel-bond can be described by the parameters of parallel-bond tensile strength, parallel-bond cohesion and parallel-bond friction angle. The detailed descriptions of the micro-parameters used in the simulations are detailed in Tab. 1. During the test, Wall #4 was fixed

and shear stress was applied by the vertical movement of the Wall #1. A displacement rate of 0.08 m/s was adopted for shear stress loading, which is low enough for a static rock loading simulation [2,28]. As this study aimed to investigate the influence of geometric dimensions of a rock disk on shear behavior and provide a recommended sample size for the PST, the confining stress applied by Wall #5 was set to zero. The PST simulations were conducted on disks with a D from 30 to 70 mm at intervals of 10 mm. The ratio between D_i and D (R_d) ranged from 0.15 to 0.75 in intervals of 0.15. The ratio between H and D_i (R_h) varied from 0.6 to 2.2 with an interval of 0.4. In addition, the bottom diameter of the surface was also defined as 4 mm larger than the applied D_i (i.e., $n = 4$ mm in Eq. (15)). Tab. 2 provides detailed descriptions of the geometric dimensions of the 125 samples used in the numerical simulations.

Table 1: Micro-parameters used for PST simulation

Micro-parameter	Value
Parallel-bond tensile strength (MPa)	4.0
Parallel-bond cohesion (MPa)	4.5
Parallel-bond friction angle (°)	42
Ratio of maximum to minimum radius of ball	1.4
Ration of normal to shear stiffness of parallel	1.5
Particle friction coefficient	0.57

Table 2: Detailed description for geometrical dimensions of the disks used for PST simulation

No.	D (mm)	R_d (%)	R_h (%)	No.	D (mm)	R_d (%)	R_h (%)	No.	D (mm)	R_d (%)	R_h (%)	No.	D (mm)	R_d (%)	R_h (%)	No.	D (mm)	R_d (%)	R_h (%)
1	30	15	60	26	40	15	60	51	50	15	60	76	60	15	60	101	70	15	60
2			100	27			100	52			100	77			100	102			100
3			140	28			140	53			140	78			140	103			140
4			180	29			180	54			180	79			180	104			180
5			220	30			220	55			220	80			220	105			220
6		30	60	31		30	60	56		30	60	81		30	60	106		30	60
7			100	32			100	57			100	82			100	107			100
8			140	33			140	58			140	83			140	108			140
9			180	34			180	59			180	84			180	109			180
10			220	35			220	60			220	85			220	110			220
11		45	60	36		45	60	61		45	60	86		45	60	111		45	60
12			100	37			100	62			100	87			100	112			100
13			140	38			140	63			140	88			140	113			140
14			180	39			180	64			180	89			180	114			180
15			220	40			220	65			220	90			220	115			220
16		60	60	41		60	60	66		60	60	91		60	60	116		60	60
17			100	42			100	67			100	92			100	117			100
18			140	43			140	68			140	93			140	118			140
19			180	44			180	69			180	94			180	119			180
20			220	45			220	70			220	95			220	120			220
21		75	60	46		75	60	71		75	60	96		75	60	121		75	60
22			100	47			100	72			100	97			100	122			100
23			140	48			140	73			140	98			140	123			140
24			180	49			180	74			180	99			180	124			180
25			220	50			220	75			220	100			220	125			220

3 Results and Analysis

3.1 Strength and Deformation

Twenty-five of the 125 samples were selected for analysis. Figs. 4a–4c give the curves with various D ($R_d = 0.45$, $R_h = 0.6$), R_d ($D = 50$ mm, $R_h = 0.6$), and R_h ($D = 50$ mm, $R_d = 0.45$), respectively. The shear stress–shear displacement curves can be divided into three stages: linear, nonlinear, and post-peak (Fig. 4). In the linear stage, shear stress exhibits linear growth as shear displacement increases. As the shear stress–shear displacement curve enters a nonlinear stage, shear stress increases nonlinearly with increased shear displacement. In the post-peak stage, the shear stress decreases gradually as the shear displacement increases. The shear stress of the samples with a higher R_h decreases more slowly, which is even more obvious in Fig. 4c. Between the linear and nonlinear stages, most of the samples have a distinct drop in shear stress, except for the sample with the $D = 50$, $R_d = 0.75$, $R_h = 0.6$, the sample with the $D = 50$, $R_d = 0.45$, $R_h = 1.8$, and the sample with the $D = 50$, $R_d = 0.45$, $R_h = 2.2$ (Figs. 4b, 4c). Shear strength and shear stiffness of samples with varying geometric dimensions differ, indicating that geometric dimensions of the sample disk have significant effects on the behavior of shear mechanics.

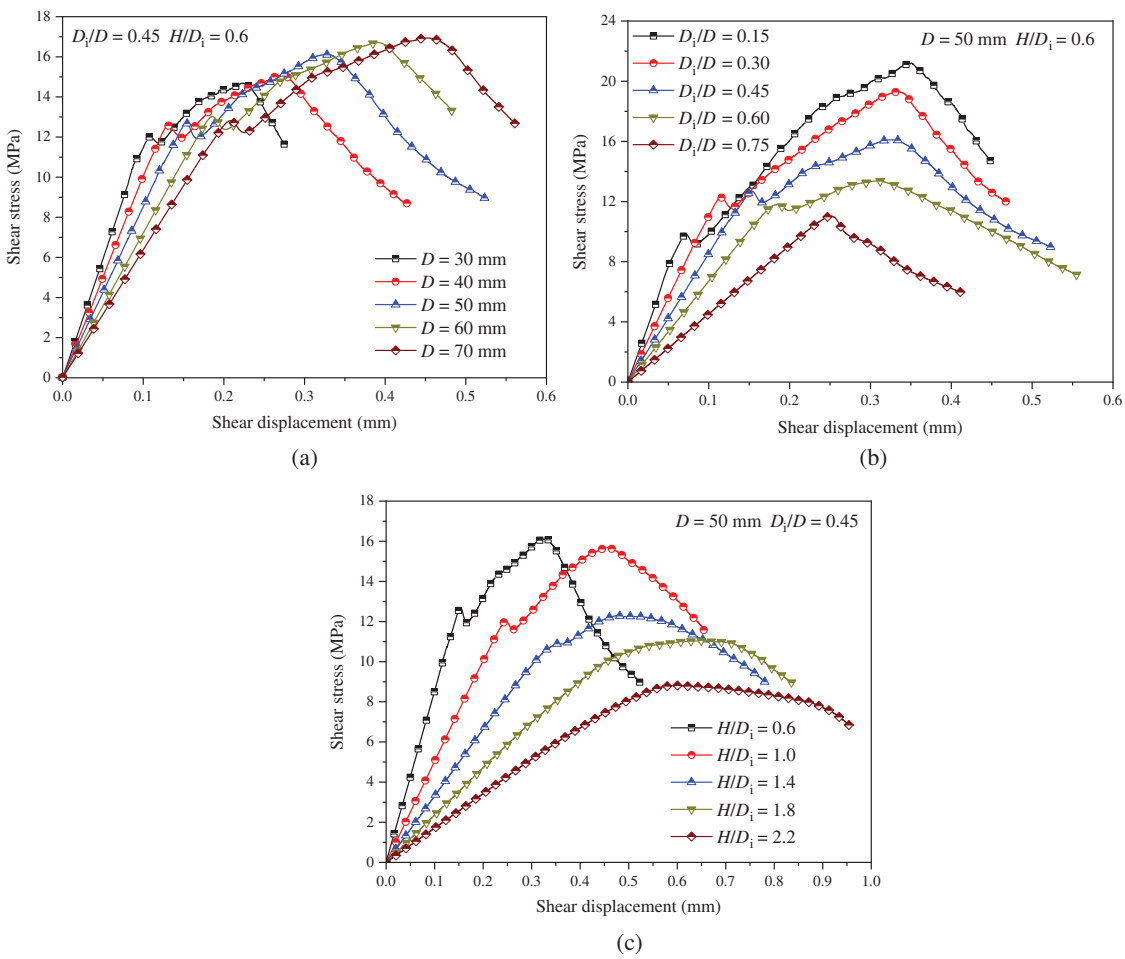

Figure 4: Shear stress–shear displacement curves of samples with (a) $R_d = 0.45$ and $R_h = 0.6$, (b) $D = 50$ mm $R_h = 0.6$, (c) $D = 50$ mm and $R_d = 0.45$

Fig. 5 shows the influence of disk geometric dimensions on the shear strength in the PST. When the R_d is equal to 0.15, the shear strength increases and then stays at a high level with the increase of the R_h except for the sample with the D equal to 30 mm, which shows a constant increase (Fig. 5a). For all of the samples with the R_d equal to 0.3, the shear strength initially grows and then declines. However, the shear strength of the samples with the R_d equal to 0.45 first increases and then decreases when the D is 30 and 40 mm (Figs. 5a and 5b), which reduces gradually when the D is in the range from 50 to 70 mm (Figs. 5c–5e). When the R_d is equal to 0.6 or 0.75, shear strength of all samples reduces gradually as the R_h grows. Shear strength gradually decreases as the R_d increases from 0.3 to 0.75 (Fig. 5). As shown in Fig. 5f, the shear strength gradually approaches a constant as the R_d and R_h increase. However, the shear strength of the samples with different D values varies little.

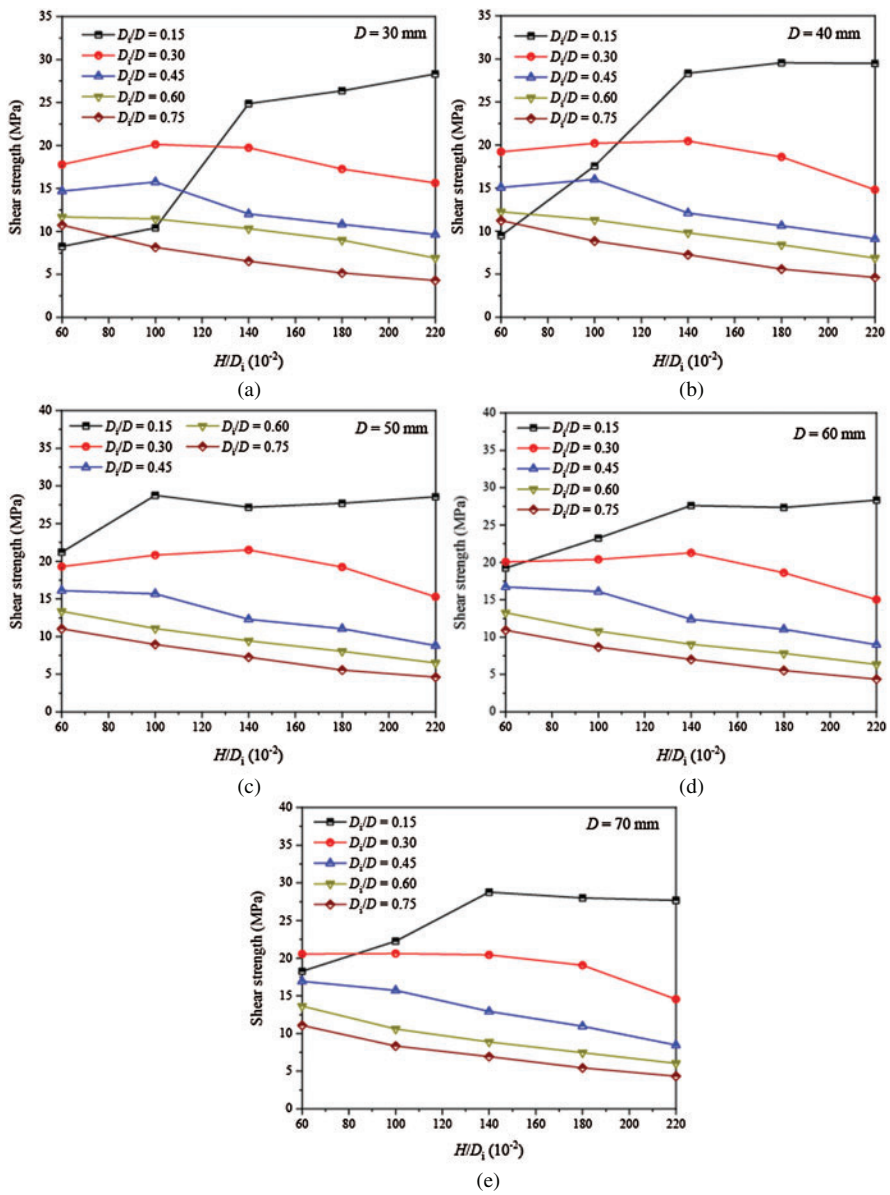

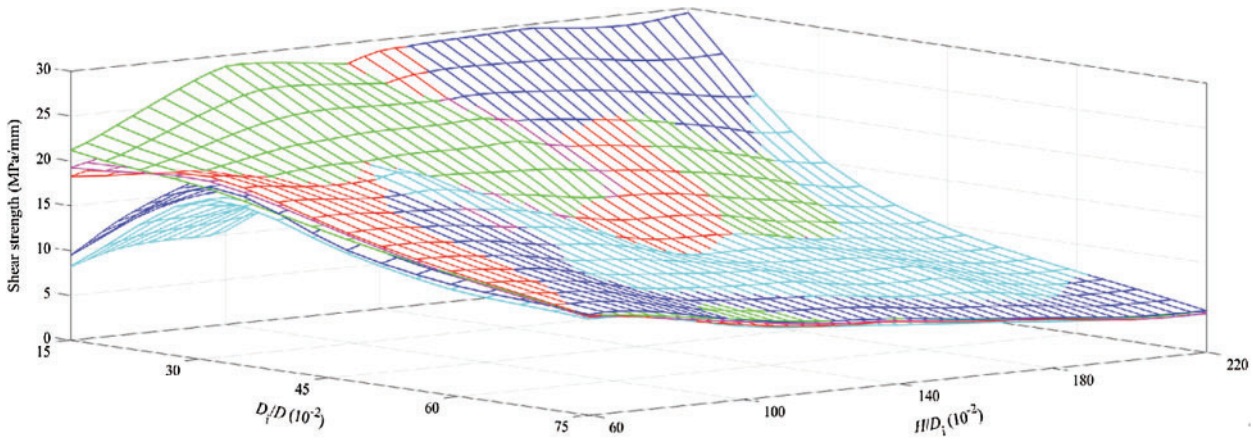

(f)

Figure 5: Shear strength of disks with various disk geometrical dimensions (a–e) are the changes in shear strength of samples with different disk diameter and (f) shows the relationship between shear strength, H/D_i and D_i/D in a three-dimensional coordinate system

In the linear stage, the shear stress increases linearly with the increase of the shear displacement (Fig. 4). The slope of this linear increase is the shear stiffness of the disk in the PST (Fig. 6). The shear stiffness decreases nonlinearly with the growth of the R_d and the R_h (Fig. 6). Additionally, it can be seen that the shear stiffness reduces gradually as the disk diameter D increases (Fig. 6b). The difference of the shear stiffness with various values of D is larger when the sample has a smaller R_d or R_h. As shown in Fig. 6a, for samples with a R_d of 0.15 and a R_h of 0.6, the maximum shear stiffness is 175.21 MPa/mm while the minimum shear stiffness is 114.85 MPa/mm. However, for the samples with a R_d of 0.75 and a R_h of 2.2, the maximum and the minimum shear stiffness are 8.21 and 3.99 MPa/mm, respectively. Thus, the shear stiffness of a sample is more sensitive to the D in the PST when the R_d and R_h is small. With the increase of the R_d and R_h, the shear stiffness gradually approaches a threshold and the difference in shear stiffness between different samples with varying D reduces (Fig. 6b), similar to the results for shear strength (Fig. 5).

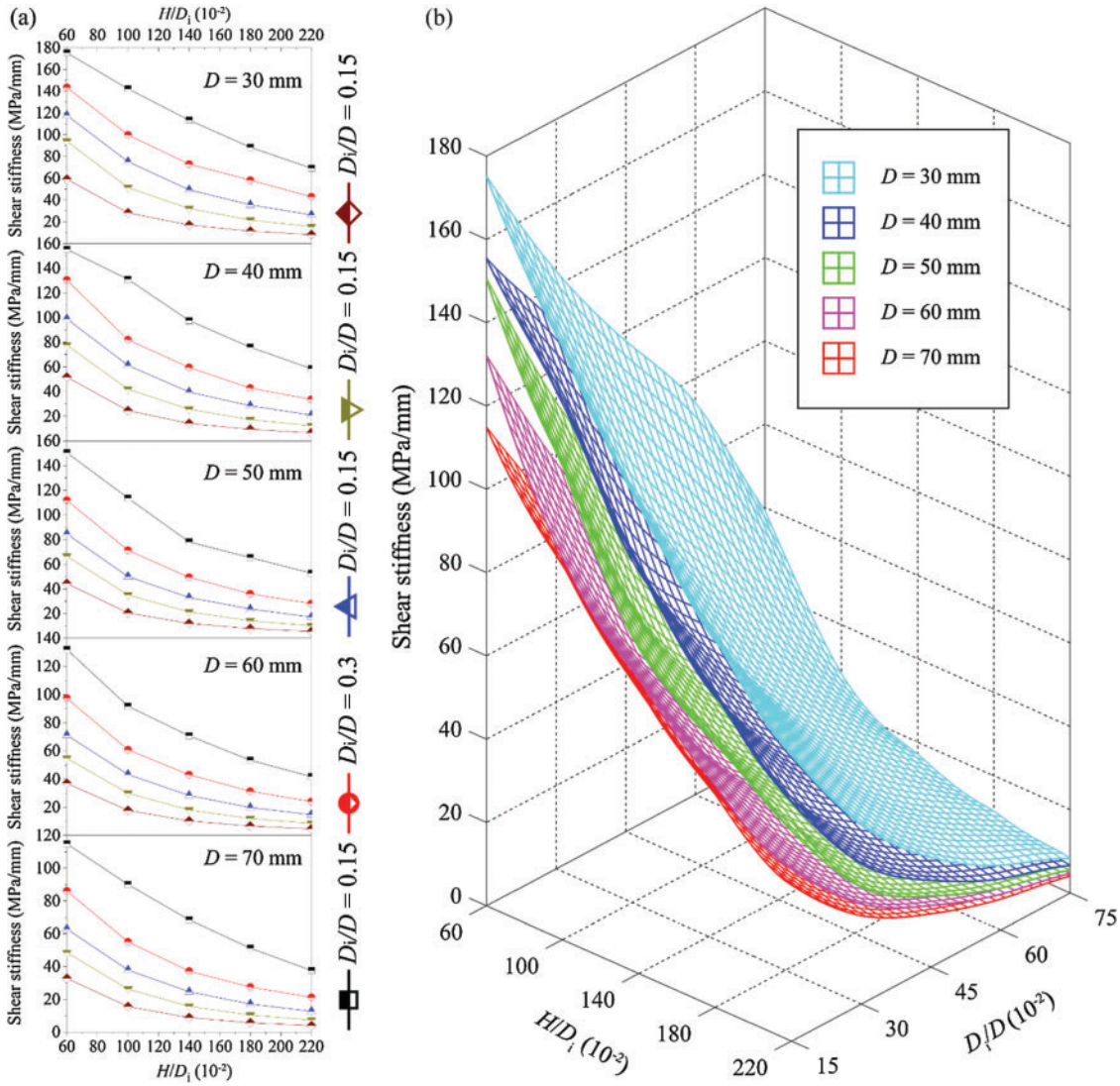

Figure 6: Change in shear stiffness of disks with various geometrical dimensions (a) shows the changes in shear stiffness of samples with different disk diameter and (b) shows the relationship between shear stiffness, H/D_i and D_i/D in a three-dimensional coordinate system

The change in normal displacement with shear displacement is shown in Fig. 7. The variation of the normal displacement can be divided into three stages: Initial stage, acceleration stage, and linear stage. In the initial stage, the normal displacement increases slowly as the shear displacement increases. It can be observed that the initial stage in Fig. 7 corresponds to the timing of the linear stage in Fig. 4. The acceleration stage is nonlinear, with the normal displacement growth rate increasing gradually. This stage corresponds to the stage near the peak shear stress of the curves in Fig. 4. In this stage, the shear stress–shear displacement changes from pre-peak to post-peak. In the linear stage in Fig. 7, the normal displacement increases linearly with the growth of the shear displacement. This stage corresponds to the post-peak stage in Fig. 4. The slope of the curve in Fig. 7 is the shear dilatancy angle of the sample in the PST. Based on these results, the change

in normal displacement with shear displacement can be simplified into the curve shown in Fig. 8. The three types of dilatancy angles are the slopes of the three stages on the curve in Fig. 7. Where the peak dilatancy angle is the slope of the normal displacement-shear displacement curve at peak shear stress.

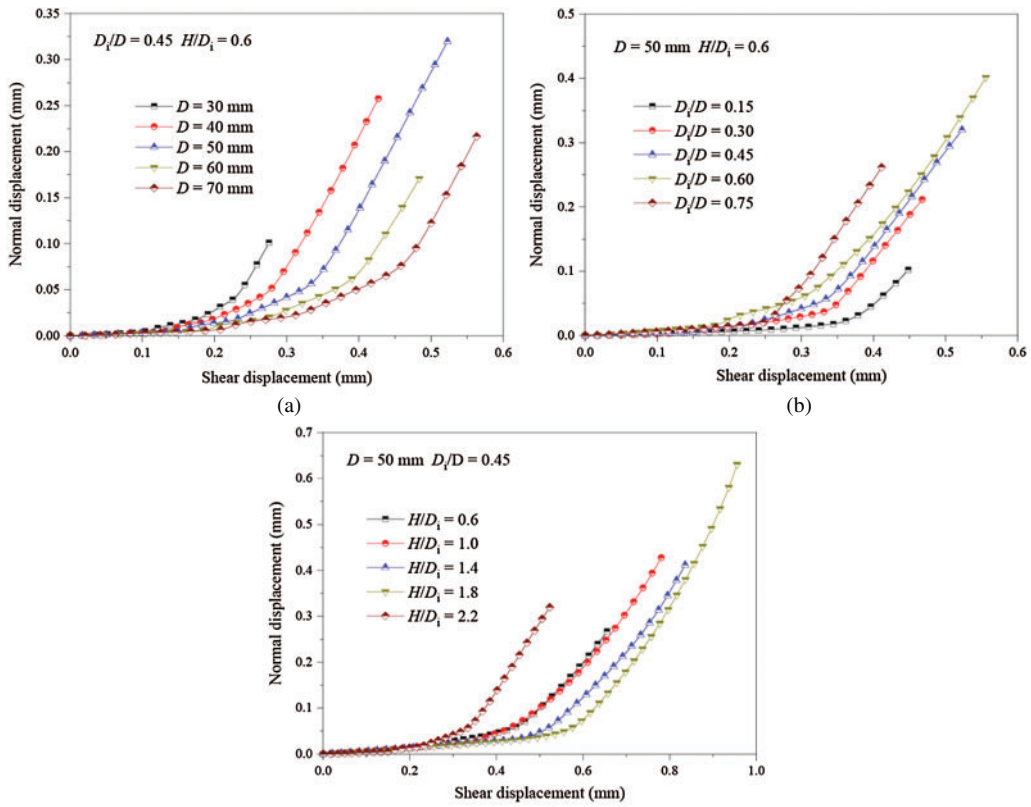

Figure 7: Normal displacement-shear displacement curves of samples with various (a) D, (b) D_i and (c) H

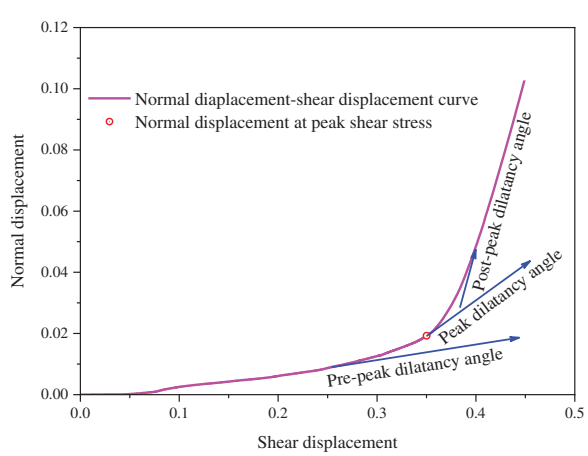

Figure 8: Three types of dilatancy angle

Fig. 9 gives the dilatancy angle of disks in the PST. The abscissa in Fig. 9a is the sample number listed in Tab. 2, in which the detailed geometric dimensions for each sample are presented. An increase in the abscissa means an increase in D, D_i, or H (Tab. 2). For the disks with the same D, the pre-peak dilatancy angle first increases and then decreases as the sample number increases in general, and all of the maximum pre-peak dilatancy angles are obtained when both R_d and R_h are equal to 0.6 (i.e., the samples numbered 16, 41, 66, 91 and 116) (Fig. 9a). The pre-peak dilatancy angle exhibits such a change due to the pre-peak dilatancy angle first growing and then reducing with the increase of the R_d under the same R_h (Fig. 9b). Meanwhile, the pre-peak dilatancy angle increases gradually with the increase of the R_h for the samples with a small R_d while that decreases as the R_h grows when the R_d is higher (Fig. 9b). For the samples with different D and the same R_h and R_d, the pre-peak dilatancy angle exhibits little difference. For example, the five maximum pre-peak dilatancy angles mentioned above are 4.58, 4.61, 4.56, 4.40, and 4.43 MPa/mm, respectively, with the difference between the maximum and the minimum value being 0.21 MPa/mm. For each sample, the peak dilatancy angle is smaller than the post-peak dilatancy angle, which can be easily understood through analyzing Fig. 8. With the increase of the sample number, the peak and post-peak dilatancy angles first increase, then remain at a high value, but in general grow slowly. The peak and post-peak dilatancy angles of the samples with a R_d of 0.15 and a R_h equal to 0.6 and 1.0 are very small compared to the other samples. Thus, the variation of the R_d and R_h has little influence on the peak and post-peak dilatancy angles except when the two parameters are small (R_d equal to 0.15 and R_h of 0.6 or 1.0). Similar to the pre-peak dilatancy angle, the peak and post-peak dilatancy angles have little difference for the samples with the same R_d, R_h but different D. Therefore, the influence of the disk diameter D on dilatancy angle is negligible.

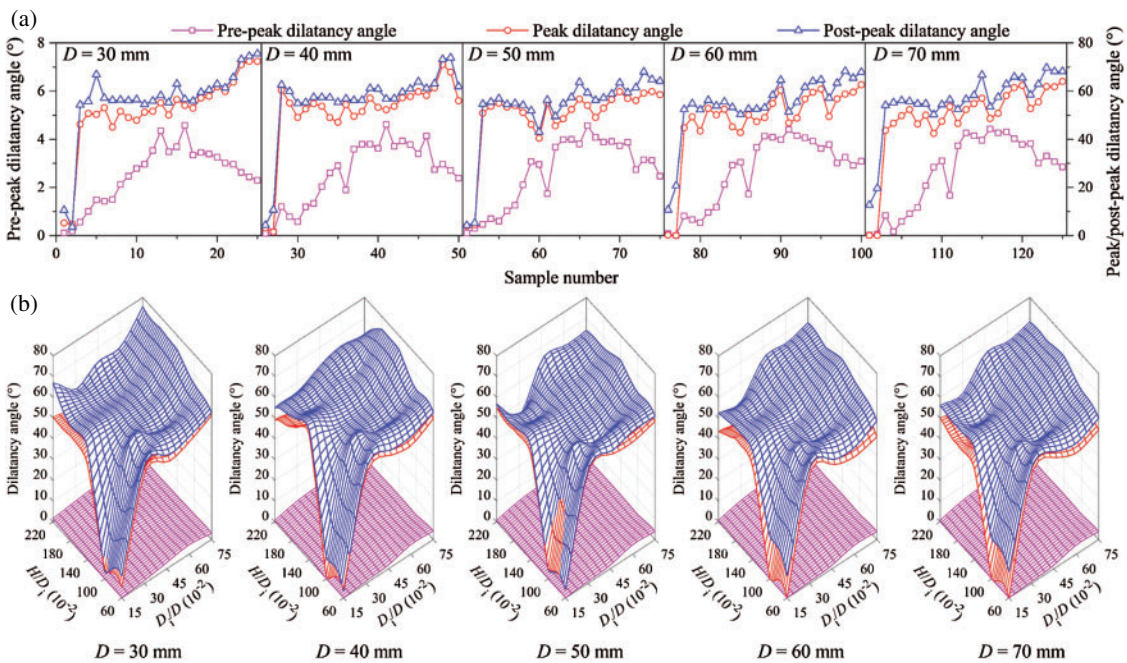

Figure 9: Change in dilatancy angles of disks in the PST (a) Shows the changes in the three types of dilatancy angles for the samples with various geometrical dimensions; (b) Shows the relationship between dilatancy angle, H/D_i and D_i/D in a three-dimensional coordinate system

3.2 Fracture Characteristic

Fig. 10 gives the fracture process of the samples with a D of 50 mm and a R_d equal to 0.3. In the same picture, the circular image on the left is the top view while the rectangular image on the right is the front view of the disk. In the top view, the larger circle is the disk outline and the smaller circle is shear surface. All pictures in the same row show the same sample (Fig. 10, rows A–E). The pictures (the top five columns on the left) in the same column show the fracture pattern of the samples under the same percent (0.2–1.0 with and interval of 0.2) of corresponding peak shear stress τ_f. The two columns on the far right show the post-peak fracture patterns of samples and their 3D view. It is worth noting that the front view of the sample is not drawn to scale for the sake of brevity and illustration. The samples have begun to crack when the shear stress reaches 0.2 τ_f (Fig. 10, column 1). Some of the cracks are near the shear surface while others appear at the edge of the sample. Cracks near the shear surface are formed due to the increase of the shear displacement and shear stress. As shear stress increases, the number of cracks near the shear surface grows significantly. However, the cracks at the edge of the sample do not expand before the pre-peak stage. At peak shear stress and in the post-peak stage, a large number of micro-cracks have been produced at the shear surface, forming multiple macro-cracks along the radial direction of the samples (Fig. 10, columns 5 and 6). The fracture pattern of the sample is very close to that in the laboratory test shown in Fig. 1b. When the R_h is less than or equal to 1.4, three macro-cracks are formed within the shear surface when the shear stress reaches $0.6\tau_f$ (Fig. 10, rows A–C, column 3). This kind of macro-crack is also produced in the sample with a R_h of 1.8 when the shear stress reaches $0.8\tau_f$ (Fig. 10, row D, column 4). Bending of the sample within the shear surface, caused by the load parallel to shear displacement, results in tensile stress on the lower surface of the sample. This is the main cause of the formation of the three macro-cracks. The three macro-cracks are produced only on the lower surface of the samples with a R_h of 1.0, 1.4, and 1.8, while they propagate to the vertical middle of the sample when the R_h is 0.6 due to the thinness of that sample. In addition, micro-cracks propagate from both vertical ends to the middle when the R_h is 0.6 and 1.0 (Fig. 10, rows A and B, column 3) while the micro-cracks propagate from one end to the other end when the R_h is 1.8 and 2.2 (Fig. 10, rows D and E, column 3).

According to Huang et al. [29], shear failure rate R_s is defined as the ratio of shear crack number to total crack number in a rock test simulation. This can be used to describe the fracture pattern. Take the samples with a D of 50 mm and a R_d of 0.6 as examples (Fig. 11). In the initial stage, the R_s fluctuates as the sample has fewer cracks and the formation of a new crack will have a significant impact on the value of R_s. After the initial fluctuations, the R_s is small (less than 0.5) and begins to increase rapidly, indicating that the sample fails due to tension in the beginning. Then, the R_s remains at a high level (greater than 0.5) before peak shear stress, indicating that the fracture of a sample is mainly caused by the formation of shear crack at this stage. In the post-peak stage, the R_s reduces gradually with the increase of the total crack number. This suggests that more tensile cracks rather than shear cracks are formed after peak shear stress.

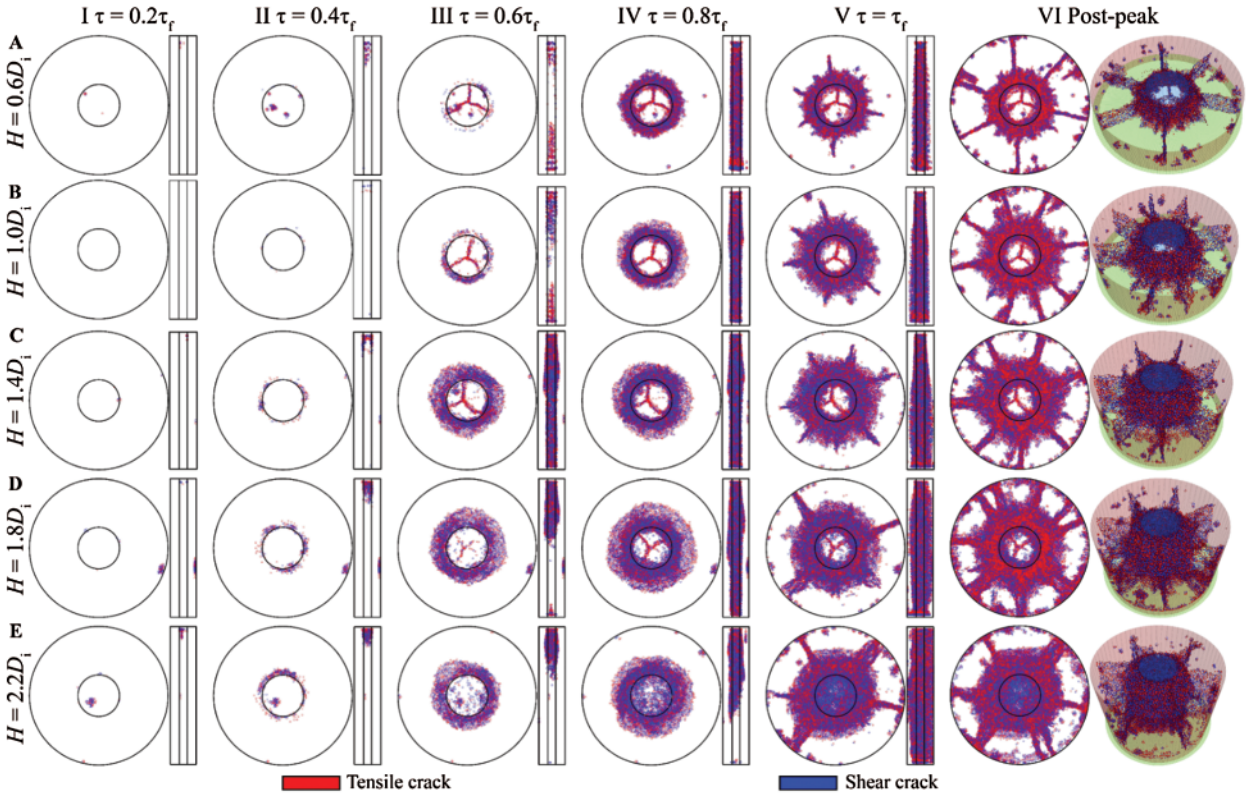

Figure 10: Fracture process of the samples with $D = 50$ mm and $R_d = 0.3$. The circular picture is the top view and the rectangular picture is the front view of disks. In the top view, the two circles are the disk outline and the shear surface, respectively. In the front view, the two vertical lines are the boundary of the shear surface

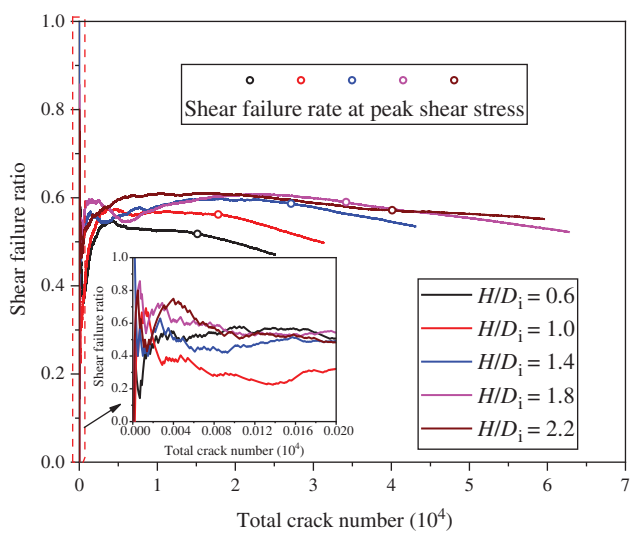

Figure 11: Change in Rs of the samples with the $D = 50$ mm and $R_d = 0.3$ and partial enlarged

Fig. 12 gives the change in peak shear failure rate (R_{sp}), which is the R_s at peak shear stress. As first introduced in Fig. 9a, the abscissa in Fig. 12a is the sample number listed in Tab. 2. On the whole, the peak shear stress gradually increases with the growth of the sample number (Fig. 12a). For the samples with a R_d of 0.15 and a R_h of either 0.6 or 1.0, the D of the sample has a marked impact on the R_{sp}. (Fig. 12a, samples 1, 2, 26, and 27) When the R_d is larger than 0.15 or the R_h is greater than 1.0, the R_{sp} remains high (greater than 0.5) and fluctuates as the sample number increases (Fig. 12b). Thus, samples mainly fail due to shear stress and the R_{sp} is not sensitive to the D when the R_d is larger than 0.15 or the R_h is greater than 1.0.

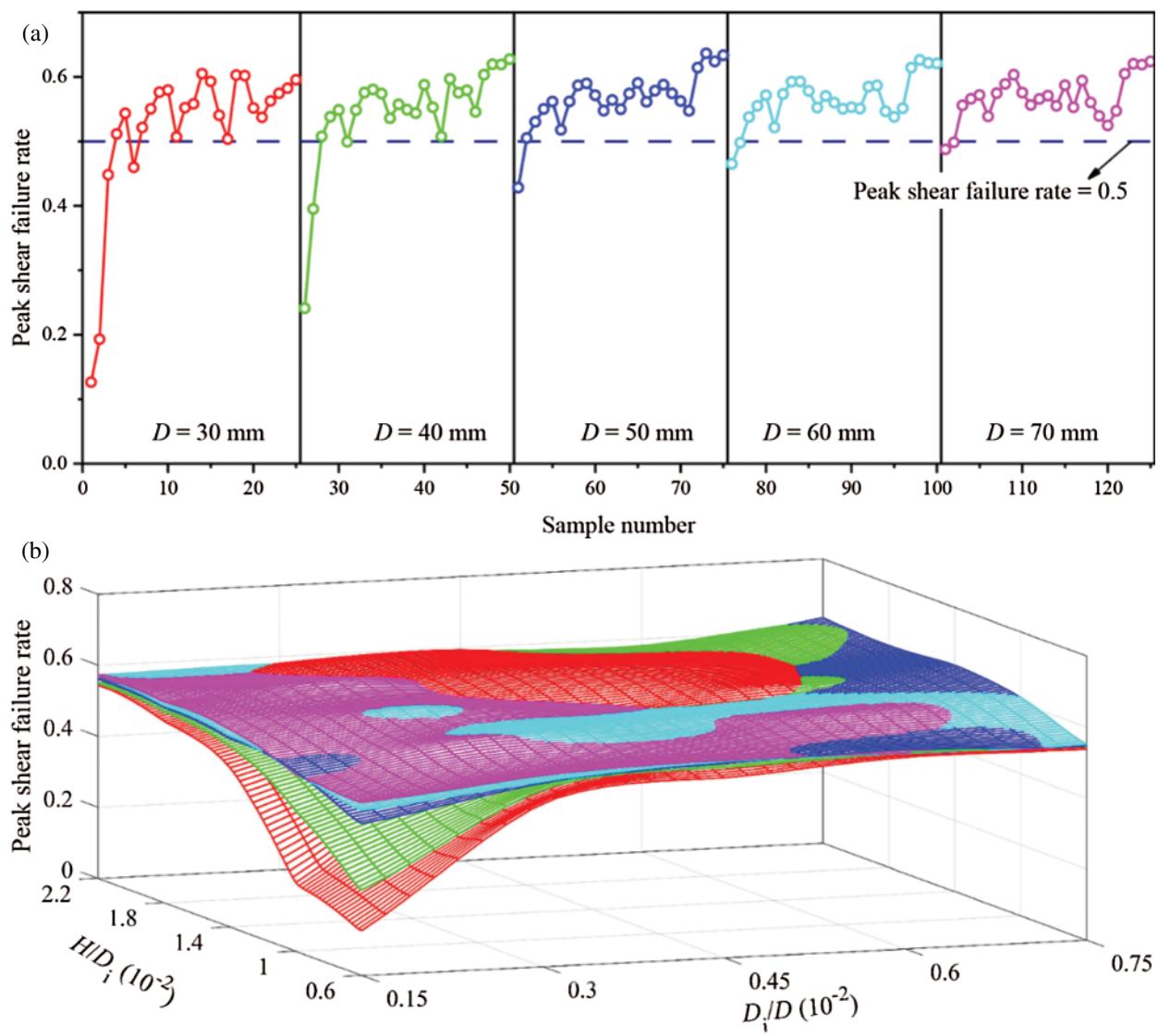

Figure 12: Change in peak shear failure rate. In which, (a) Displays the change of peak shear failure rate in a two-dimensional coordinate system, and (b) Displays the change of that in a three-dimensional coordinate system

As shown in Fig. 13, bonds in the PFC model consist of two ends, with each end connecting with a piece. The angle between the vector along each bond and the positive direction of the z-axis is β, the angle between the shear stress and the bond. To analyze the distribution of β of bonds that have failed at peak shear stress, the number of cracks per degree interval was counted. As shown in Fig. 14, the top half of each image is the proportion of cracks at a certain angle range (R_c). For example, the R_c at the degree of 1° denotes the ratio of the number of cracks with $0° \leq \beta < 1°$ to the total crack number. The bottom half of each figure in Fig. 14 is the R_{sp} of cracks within a certain angle range with the count method being the same as above. As shown in Fig. 14, which gives the change in R_c and R_{sp} of the samples with a D of 50 mm and a R_d of 0.3, the R_c is based on $\beta = 90°$ as the symmetry line. With the increase of the R_h, the curve of R_c changes from lanky to chubby. The β accounts for the largest proportion near 90°, but the maximum R_c gradually reduces as the R_h increases. The maximum R_c is 1.94% when the R_h is 0.6 (Fig. 14a), but it is 1.37% when the R_h is 2.2 (Fig. 14e), with a reduction of 29.38%. When the β is near 0° or 180°, the R_c approaches zero. This denotes that the bonds rarely fail in the PST if they are parallel to or nearly parallel to the shear direction before shear stress reaches peak value. When the R_h is small, the β has a significant impact on the R_{sp}. For the sample with a D equal 50 mm, a R_d of 0.3, and a R_h of 0.6, R_{sp} is greater than others if $0° < \beta < 25°$ or $75° < \beta < 105°$ or $155° < \beta < 180°$ (Fig. 14a). These bonds are approximately parallel or perpendicular to the shear direction. Under the action of shear displacement, either a large shear stress or a large tensile stress acts on these bonds. The shear strength of a bond is small if it is subjected to a large tensile stress (shear strength of the bond conforms to Mohr–Coulomb criterion in the PFC). So, those bonds either are subjected to a large shear stress or have a small shear strength. As a result, they are prone to fail caused by shear stress. However, the influences of β on R_{sp} have a marked reduction with the increase of the R_h. For example, the R_{sp} of the sample with a D of 50 mm, a R_d of 0.3 and a R_h of 2.2 is always about 0.6 (Fig. 14e).

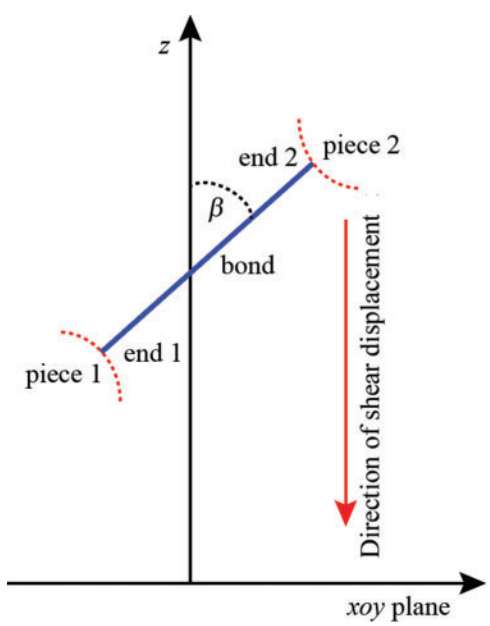

Figure 13: Schematic diagram of a bond in coordinate system

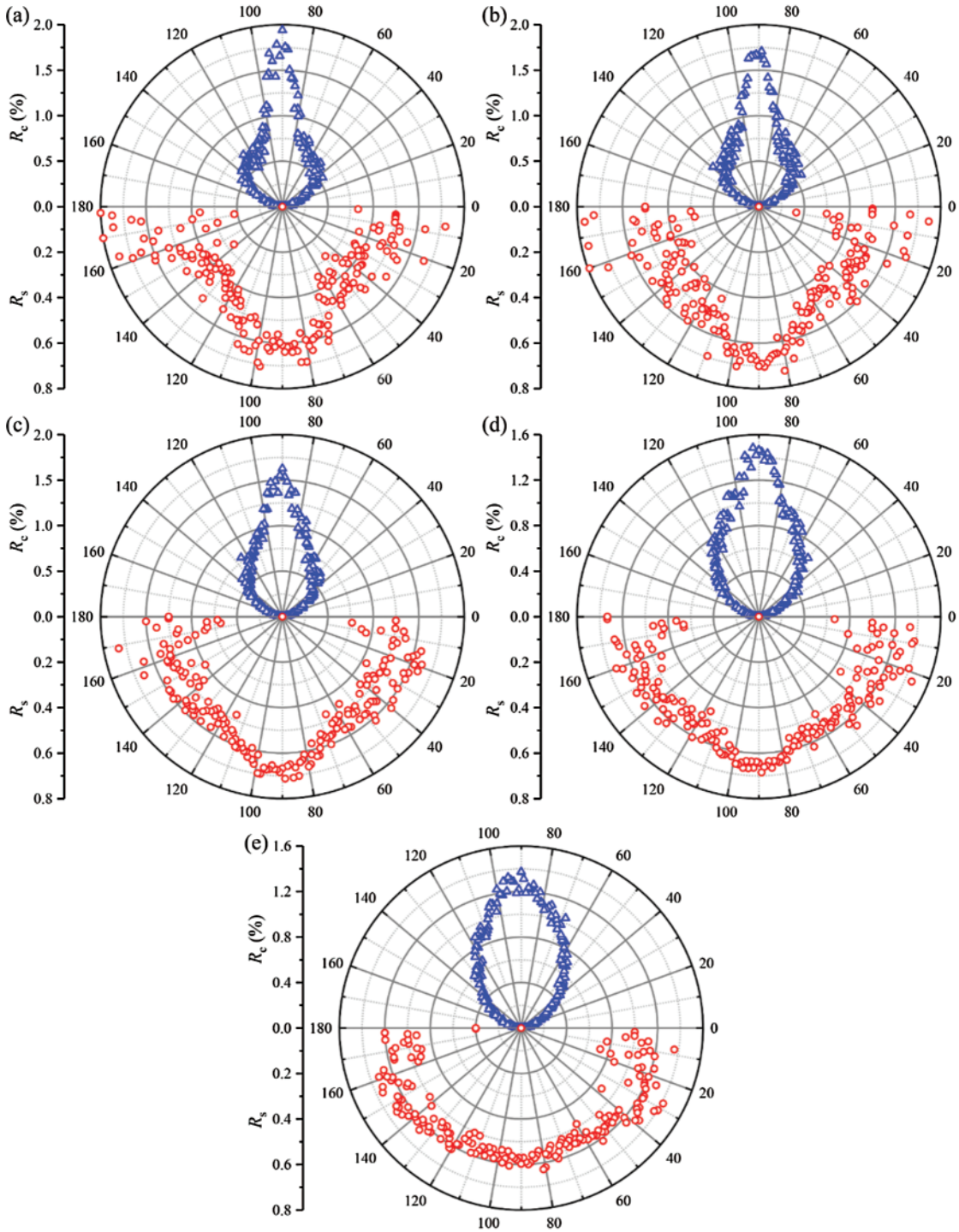

Figure 14: Change in R_c and R_s, in which the samples geometrical dimensions are $D = 50$ mm, $R_d = 0.3$ and (a) $R_h = 0.6$, (b) $R_h = 1.0$, (c) $R_h = 1.4$, (d) $R_h = 1.8$, (e) $R_h = 2.2$

4 Discussion

4.1 Normal Stress during Test

As shown in Fig. 15a sample used in the PST can be divided into two parts. Part I is the part outside the shear surface of the sample, which is a ring. Part II is the part within the shear surface of the sample. It can be known from Fig. 7 that the normal displacement increases with the increase of shear displacement, namely shear dilatancy occurs. Thus, the inner and outer diameters of Part I will grow during the test as the shear displacement increases due to shear dilatancy. Part I is subjected to tensile stress and tensile deformation in the direction perpendicular to the radial direction at any point. Additionally, Part I is subjected to compressive stress from Part II as well. Therefore, the actual normal stress on the shear surface is greater than zero in this study. If the PST is carried out under confining stress (normal stress) σ_n, the actual normal stress will be greater than σ_n. This can also be observed in Fig. 16, which shows the force chain of the contacts. When τ equals 0.6 τ_f, Part II is mainly subjected to compression while Part I is subjected to tensile in tangential direction and compressive stress in radial direction (Fig. 16a). With the increase of shear stress, the number of the contacts subjected to tensile stress grows. When τ is equal to τ_f, Part I is mainly subjected tensile stress (Fig. 16c). Thus, the disk looks like a rubber band (Part I) on a cylinder (Part II). The rubber band is stretched and applies a pressure on the cylinder. However, when the shear stress reaches its peak value, as shown in Fig. 10, macro-cracks within Part I in the radial direction have formed. At this moment, a portion of the tensile and compressive stress that Part I is subjected to in the tangential and radial directions have been released. As we know, shear strength under direct shear test is positively correlated with normal stress. Thus, the shear strength obtained by the PST will be larger than the actual shear strength, but the specific difference between the PST and real shear strength is uncertain, so further research is needed.

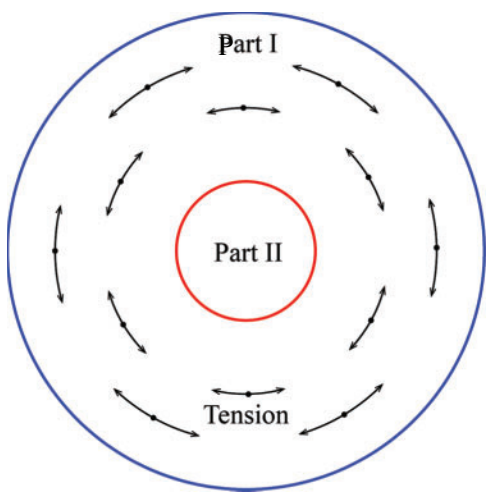

Figure 15: Stress state of a disk in the PST

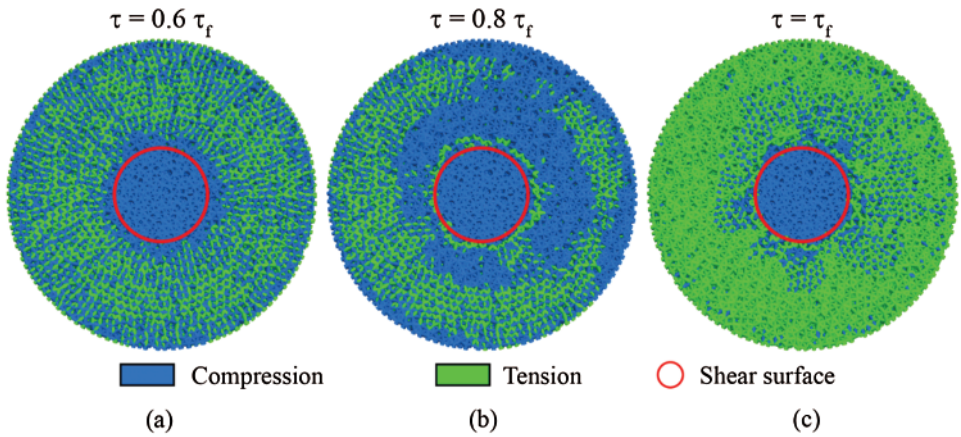

Figure 16: Force chain of the disk with $D = 50$ mm, $R_d = 0.3$ and $R_h = 1.0$ under (a) $\tau = 0.6\tau_f$, (b) $\tau = 0.8\tau_f$ and (c) $\tau = \tau_f$

4.2 Recommended Disk Geometric Dimension

Fig. 5 gives the shear strength of sample with different D, R_d and R_h. When the R_d or R_h is small, shear strength is sensitive to all the three geometric parameters. Additionally, the shear dilatancy angles (Fig. 9) and peak shear failure rate (Fig. 12) also show a great difference. Thus, in the PST, samples with a small R_d (less than 0.3) and R_h (less than 1.4) is not recommended. When the R_d is greater than 0.6, the D has little influence on the shear strength which changes little and approaches a threshold value. However, if a sample has a R_d approaching 1.0, a too small R_h, or a too large D, it will make the Part II of the sample in Fig. 15 more likely to bend or break as shown in Fig. 10. In addition, a larger R_h leads to the sample cracking from one end to the other rather than from both ends to the middle (as shown in Fig. 10, row E). From this study, the sample size that should be used for the PST should be of a D between 50 and 70 mm, a R_d between 0.45 and 0.6, and a R_h between 1.4 and 1.8. Therefore, we suggest using samples with a D of about 60 mm, a R_d of about 0.5 and a R_h of about 1.6 to carry out the PST.

5 Conclusions

The PST has been used by researchers to determine the shear mechanical parameters of rocks. However, there are no suggested sample geometric dimensions at present. Simulations using PFC3D were carried out to investigate the influences of sample geometric dimensions on shear behaviors in the PST. We found that:

(1) When the ratio between sample D_i and D or the ratio between sample H and D_i is small, shear mechanical parameters of samples, such as shear strength, shear stiffness, dilatancy angles, and shear failure rate are sensitive to the sample geometric dimensions.
(2) In the PST, a cylindrical shear surface will be formed. If the disk height is comparatively small or the diameter of the surface is comparatively larger, the sample can easily produce a tensile fracture within the shear surface. Samples with a small ratio between sample H and D_i cracks from both ends towards the middle while it cracks from one end to the other end for the samples with a large ratio between sample H and D_i.
(3) In the PST, the actual normal stress is greater than the set value, which results in larger shear strength. The suggested sample geometric dimensions are given as a D of 60 mm, a ratio between sample D_i and D of 0.5, and a ratio between sample H and D_i of 1.6.

Funding Statement: This work is supported by the Fundamental Research Funds for the Central Universities, CHD (Nos. 300102210307, 300102210308), the National Natural Science Foundation of China (Nos. 51708040, 41831286, 51678063, 51978065).

Conflicts of Interest: The authors declare that they have no conflicts of interest to report regarding the present study.

References

1. Usefzadeh, A., Yousefzadeh, H., Salari-Rad, H., Sharifzadeh, M. (2013). Empirical and mathematical formulation of the shear behavior of rock joints. *Engineering Geology, 164,* 243–252. DOI 10.1016/j.enggeo.2013.07.013.
2. Huang, D., Zhu, T. (2019). Experimental study on the shear mechanical behavior of sandstone under normal tensile stress using a new double-shear testing device. *Rock Mechanics and Rock Engineering, 52(9),* 3467–3474. DOI 10.1007/s00603-019-01762-3.
3. Kim, T., Jeon, S. (2019). Experimental study on shear behavior of a rock discontinuity under various thermal, hydraulic and mechanical conditions. *Rock Mechanics and Rock Engineering, 52(7),* 2207–2226. DOI 10.1007/s00603-018-1723-7.
4. Yin, Q., Ma, G., Jing, H., Wang, H., Su, H. et al. (2017). Hydraulic properties of 3D rough-walled fractures during shearing: An experimental study. *Journal of Hydrology, 555,* 169–184. DOI 10.1016/j.jhydrol.2017.10.019.
5. Zhu, T., Huang, D. (2019). Experimental investigation of the shear mechanical behavior of sandstone under unloading normal stress. *International Journal of Rock Mechanics and Mining Sciences, 114,* 186–194. DOI 10.1016/j.ijrmms.2019.01.003.
6. Girgin, Z. C., Arioglu, N., Arioglu, E. (2007). Evaluation of strength criteria for Very-High-Strength-Concretes under triaxial compression. *ACI Structural Journal, 104(3),* 278–284. DOI 10.1002/tal.311.
7. Li, L. R., Deng, J. H., Liu, J. F., Zheng, J., Deng, C. F. (2017). A new understanding of punch-through shear testing. *Géotechnique Letters, 7(2),* 1–7. DOI 10.1680/jgele.16.00123.
8. Zeng, B., Huang, D., Ye, S., Chen, F., Tu, Y. (2019). Triaxial extension tests on sandstone using a simple auxiliary apparatus. *International Journal of Rock Mechanics and Mining Sciences, 120,* 29–40. DOI 10.1016/j.ijrmms.2019.06.006.
9. Seidel, J. P., Haberfield, C. M. (2002). Laboratory testing of concrete-rock joints in constant normal stiffness direct shear. *Geotechnical Testing Journal, 25(4),* 391–404. DOI 10.1520/GTJ11292J.
10. Park, J. W., Song, J. J. (2009). Numerical simulation of a direct shear test on a rock joint using a bonded-particle model. *International Journal of Rock Mechanics and Mining Sciences, 46(8),* 1315–1328. DOI 10.1016/j.ijrmms.2009.03.007.
11. Wang, J. J., Guo, J. J., Bai, J. P., Wu, X. (2018). Shear strength of sandstone–mudstone particle mixture from direct shear test. *Environmental Earth Sciences, 77(12),* 442–441. DOI 10.1007/s12665-018-7622-0.
12. Yin, Q., Jing, H. W., Meng, B., Liu, R. C., Wu, J. Y. (2020). Shear mechanical properties of 3D rough-walled rock surfaces under constant normal stiffness conditions. *Chinese Journal of Rock Mechanics and Engineering, 39(11),* 2213–2225. DOI 10.13722/j.cnki.jrme.2020.0259 (in Chinese).
13. Xu, M., Song, E., Chen, J. (2012). A large triaxial investigation of the stress-path-dependent behavior of compacted rockfill. *Acta Geotechnica, 7(3),* 167–175. DOI 10.1007/s11440-012-0160-0.
14. Zhang, H. Q., Tannant, D. D., Jing, H. W., Nunoo, S., Niu, S. J. et al. (2015). Evolution of cohesion and friction angle during microfracture accumulation in rock. *Natural Hazards, 77(1),* 497–510. DOI 10.1007/s11069-015-1592-2.
15. Ge, Y., Tang, H., Eldin, M. A. M. E., Wang, L., Wu, Q. et al. (2017). Evolution process of natural rock joint roughness during direct shear tests. *International Journal of Geomechanics, 17(5),* 1–10. DOI 10.1061/(ASCE)GM.1943-5622.0000694.

16. Wang, P., Ren, F., Miao, S., Cai, M., Yang, T. (2017). Evaluation of the anisotropy and directionality of a jointed rock mass under numerical direct shear tests. *Engineering Geology, 77(12),* 1–12. DOI 10.1016/j.enggeo.2017.03.004.
17. Stacey, T. R. (1980). A simple device for the direct shear-strength testing of intact rock. *Journal of the South African Institute of Mining and Metallurgy, 80,* 129–130. DOI 10.1016/0022-5088(80)90299-4.
18. Sulukcu, S., Ulusay, R. (2001). Evaluation of the block punch index test with particular reference to the size effect, failure mechanism and its effectiveness in predicting rock strength. *International Journal of Rock Mechanics and Mining Sciences, 38(8),* 1091–1111. DOI 10.1016/S1365-1609(01)00079-X.
19. Yoon, J., Jeon, S. (2004). Experimental verification of a (punch through shear) PTS mode II test for rock. *International Journal of Rock Mechanics and Mining Sciences, 41(3),* 353–354. DOI 10.1016/j.ijrmms.2003.12.060.
20. Wu, H., Kemeny, J., Wu, S. (2017). Experimental and numerical investigation of the punch-through shear test for mode II fracture toughness determination in rock. *Engineering Fracture Mechanics, 184,* 59–74. DOI 10.1016/j.engfracmech.2017.08.006.
21. Li, Z., Nguyen, T. S., Su, G., Labrie, D., Barnichon, J. D. (2017). Development of a viscoelastoplastic model for a bedded argillaceous rock from laboratory triaxial tests. *Canadian Geotechnical Journal, 54(3),* 359–372. DOI 10.1139/cgj-2016-0100.
22. Xu, Y., Yao, W., Xia, K., Ghaffari, H. O. (2019). Experimental study of the dynamic shear response of rocks using a modified punch shear method. *Rock Mechanics and Rock Engineering, 52(8),* 2523–2534. DOI 10.1007/s00603-019-1744-x.
23. Huang, S., Feng, X. T., Xia, K. (2011). A dynamic punch method to quantify the dynamic shear strength of brittle solids. *Review of Entific Instruments, 82(5),* 165. DOI 10.1063/1.3585983.
24. Backers, T., Stephansson, O., Rybacki, E. (2002). Rock fracture toughness testing in mode II—punch-through shear test. *International Journal of Rock Mechanics and Mining Sciences, 39(6),* 755–769. DOI 10.1016/S1365-1609(02)00066-7.
25. Zhang, X. P., Wong, L. N. Y. (2013). Crack initiation, propagation and coalescence in rock-like material containing two flaws: A numerical study based on bonded-particle model approach. *Rock Mechanics Rock Engineering, 46(5),* 1001–1021. DOI 10.1007/s00603-012-0323-1.
26. Yang, S. Q. (2015). Discrete element modeling on fracture coalescence behavior of red sandstone containing two unparallel fissures under uniaxial compression. In: *Strength failure and crack evolution behavior of rock materials containing pre-existing fissures*. vol. 178, pp. 28–48, Berlin Heidelberg: Springer.
27. Wei, M. D., Dai, F., Xu, N. W., Zhao, T., Liu, Y. (2017). An experimental and theoretical assessment of semi-circular bend specimens with chevron and straight-through notches for Mode I fracture toughness testing of rocks. *International Journal of Rock Mechanics and Mining Sciences, 99,* 28–38. DOI 10.1016/j.ijrmms.2017.09.004.
28. Bahaaddini, M., Hagan, P. C., Mitra, R., Hebblewhite, B. K. (2014). Scale effect on the shear behaviour of rock joints based on a numerical study. *Engineering Geology, 181,* 212–223. DOI 10.1016/j.enggeo.2014.07.018.
29. Huang, D., Zhu, T. T. (2018). Experimental and numerical study on the strength and hybrid fracture of sandstone under tension-shear stress. *Engineering Fracture Mechanics, 200,* 387–400. DOI 10.1016/j.engfracmech.2018.08.012.